

GT2011-45127

Design considerations for axial steam turbine rotor inlet cavity volume and length scale

Konstantinos G. Barmpalias, Anestis I. Kalfas¹, Reza S. Abhari,
Laboratory for Energy Conversion
Department of Mechanical and Process Engineering
ETH Zurich
Zurich, Switzerland

Toshio Hirano, Naoki Shibukawa
Kehin Product Operations, Toshiba Corporation
Power and Industrial Systems R & D center, Toshiba Corporation

Takashi Sasaki
Thermal and Hydro Power Systems and Services Division
Toshiba Corporation, 105-8001 Tokyo, Japan

ABSTRACT

In this paper we examine the interaction between the cavity and main flows of three different rotor cavities. For each of the three rotor cavities, the cavity inlets differ in their axial cavity lengths, which are modified by extending the upper casing stator platform. The three cavity volumes are comprised of a baseline case, along with a 14% and a 28% volume reduction relative to the baseline case. Measurements show that there is an increase in efficiency of 0.3% for the 14% cavity volume reduction case (relative to the baseline case), whereas a further volume reduction of 28% (relative to the baseline case) decreases the efficiency. Computational analysis highlights the break-up of a toroidal vortex within the cavity as the primary factor explaining the changes in efficiency. The dominant cavity vortex originally present in the baseline case firstly broken up into two smaller vortices for the 14% cavity volume reduction case and secondly, completely replaced with a strong radial jet for the 28% volume reduction case. From a design perspective, reducing the cavity volume by extending the upper casing stator platform yields improvements in efficiency provided that the cavity vortex is still present. The design considerations, analysis and the associated aerodynamics are discussed in detail within this paper.

INTRODUCTION

Leakage flow in shrouded turbines has recently received much attention from turbine designers. The pressure difference across the rotor drives the leakage flow across the

labyrinth and over the rotor. This leakage flow produces no work on the rotor and thus is a source of loss. Furthermore, the leakage flow exiting the labyrinth, either downstream of the stator or the rotor, causes extensive mixing in the interaction zone and induces a more negative incidence (relative to the main flow) on the downstream blade row, thereby incurring more losses. Therefore, it is of interest to develop methods to mitigate the adverse effects of leakage flows on the turbine's efficiency. Using theoretical and experimental approaches, Egli [1], and Traupel [2] attempted to quantify the leakage mass flow through the labyrinth seal of shrouded turbines. Wallis et al. [3] noted four loss-generating mechanisms; a) fluid that enters the shroud cavity; b) mixing in the clearance downstream of the fin; c) mixing with the mainstream flow and d) non-ideal incidence on the downstream blade row. They concluded that modern sealing arrangements have already reached their efficiency limits and that further improvement can only be achieved by controlling the leakage flow itself. Rosic and Denton [4] used bladelets on the downstream radial wall of the cavity to control the leakage flow during re-entry from the exit cavity. Using a similar approach, Mahle [5] reported marginal efficiency gains in a computational study. The mixing loss during re-entry has been identified by Denton [6] as the main entropy-creating process in his work on loss mechanisms in turbomachines. Peters et al. [7], Anker et al. [8] and Gier et al. [9] reported on the strong interactions between cavity and main flow and examined the different loss-generating mechanics. They discussed the secondary channel vortex and its strengthening due to the egress of the cavity flow. On the same topic, Pau et al. [10] studied the impact of the leakage flow on the main flow. They showed

¹Current address: Aristotle University of Thessaloniki, Greece

that there is an enhancement of all counter-rotating vortices with respect to the main passage vortex due to the low turning that is experienced by the leakage flow. The strong negative vorticity that dominates the secondary flows at the interaction zone has also been reported by Adami et al. [11]. Cavity flows also have a strong impact on the downstream blade rows. Hunter and Manwaring [12] reported in detail on the effect of hub leakage flow on secondary flow structures downstream of the rotor and stator. With the use of ethylene tracer gas, they traced the low momentum fluid generated by the mixing of the cavity and main flows at the downstream rotor row. They also traced two additional vortices in the following stator passage, which are associated with the total pressure deficit and the radial variation in circumferential flow angle of the upstream rotor. Although modern sealing has reached high levels of effectiveness, some work in this area has recently been undertaken by Vakili et al. [13]. They studied seal designs to examine their influence on leakage characteristics. PIV measurements and computational analysis were used to assess the effectiveness of the fin axial location and angle, and the step height on leakage flow reduction. Flow visualization was also used by Rhode et al. [14], [15] in their water test facility to measure leakage resistance with regard to step shape and height. Curtis et al. [16] showed the potential to reduce or even eliminate leakage flow using a different approach with no seals, by using an air curtain with a flow that was injected backwards angled at 45 degrees to the axial direction. With the use of inserts, Schlienger et al. [17] attempted to improve re-entry of the leakage flow, but they surprisingly showed a decrease in efficiency. Pfau et al. [18], [19] systematically investigated cavity flows in different cavity configurations. They described in detail the toroidal vortex as the dominant kinematic flow feature in the cavity region. The toroidal vortex is fed with high-pressure fluid from the pressure side of the stator blade. The associated fluctuating mass, generated by the in and outflows due to the upstream stator exit pressure field and the downstream rotor potential flow field, in turn results in negative incidence on the rotor. They made some design recommendations based on the secondary flow development and mixing losses at the inlet and exit cavity which were due to the interaction between the cavity and main flows.

The modification of the dominant vortex in the inlet cavity and the reinjection of leakage flow into the main flow has been the primary focus of modern sealing techniques. However, it is evident that further work is required to identify the optimum inlet cavity flow field mechanisms in order to yield an overall improvement in efficiency. In the present work this is examined in an experimental study of different inlet cavity configurations. In these configurations the cavity volume is systematically varied. The flow field measurements are complemented by computational analysis that is used to further detail the characteristics of the flow field. It is demonstrated that by closely considering the cavity volume and length, a gain in efficiency of up to 0.3% can be achieved.

NOMENCLATURE

c	normalized cavity axial length
C_{pt}	pressure coefficient $(P_t - P_{s,exit}) / (P_{t,inlet} - P_{s,exit})$
h	normalized blade span
P	pressure
R1	1 st rotor
R2	2 nd rotor
S1	1 st stator
S2	2 nd stator
y^+	dimensionless wall distance
z	axial direction

Greek

α	absolute flow yaw angle
γ	flow pitch angle

Subscript

s	static
t	total

Abbreviations

CFD	computational fluid dynamics
CV	cavity volume
CVR	cavity volume reduction
EXP	experiment
HS	high solidity
LS	low solidity
PIV	particle image velocimetry
Δ_{eff}	efficiency difference

INLET CAVITY CONFIGURATIONS

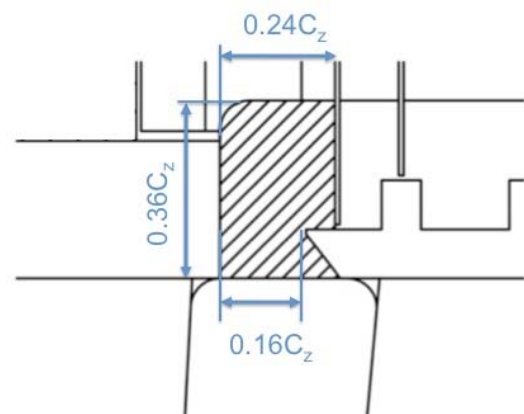


Figure 1: Illustration of the inlet cavity (Baseline Case – Configuration).

The research turbine under examination has a sealing configuration of 4 seals with a gap of 0.44% of the blade span. The inlet cavity under investigation is the one illustrated in Figure 1 and corresponds to the baseline case. The dimensions are $0.24C_z$ and $0.36C_z$, in the axial and

radial directions respectively, which provides a minimum operating safety distance of $0.16C_z$ between the rotor shroud and stator casing. In addition to the baseline case, two more cases were examined in this study and are shown in Figures 2a and 2b. The cavity sizes are 14% and 28% smaller than the baseline case (Figure 1). The volume reduction is accomplished by an extension of the upper stator casing platform to reduce the cavity's axial length by 17% and 34%, respectively (Figures 2a and 2b). The extension is depicted in red in Figure 2.

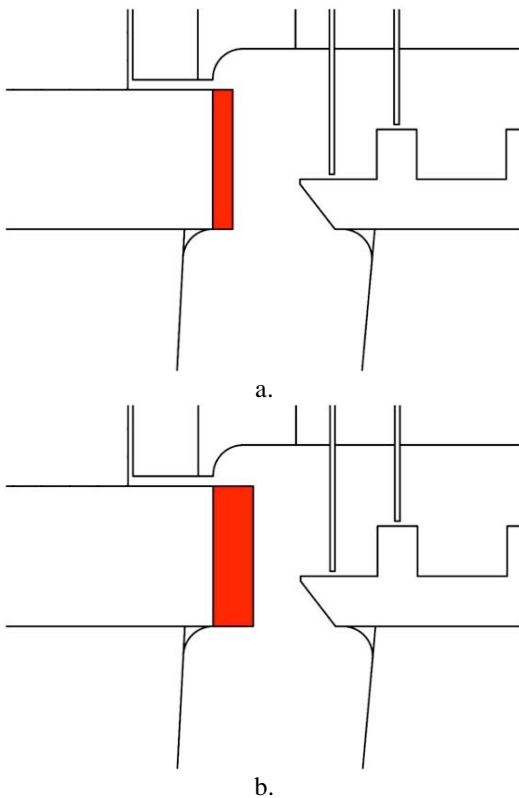


Figure 2: Extension of the upper casing stator platform by a. 17% and b. 34% of the cavity's axial length.

EXPERIMENTAL METHOD

The research facility

The measurements were performed in the 'LISA' two-stage axial research turbine at the Laboratory for Energy Conversion (LEC) of ETH Zurich. The turbine inlet temperature (TIT) is kept constant at 310 K, with an accuracy of 0.9 K. A DC generator maintains a constant operating speed of 2750 ± 0.5 RPM ($\pm 0.02\%$). The measurement uncertainty of the test facility concerning total-to-static efficiency of the second stage is $\pm 0.21\%$. A more detailed description of the test facility is available in Schlienger et al. [20]. The stator blade row configurations

differ as shown in Table 1. The first stator is of a high solidity ($\sigma = 1.43$) design, whereas the second stator has a low solidity ($\sigma = 1.25$). Both stators are designed to have the same exit flow angle and axial chord. The associated operating parameters based on the LS stator are summarized in Table 2. More detailed measurements on the baseline test case can be found in Tashima et al. [21].

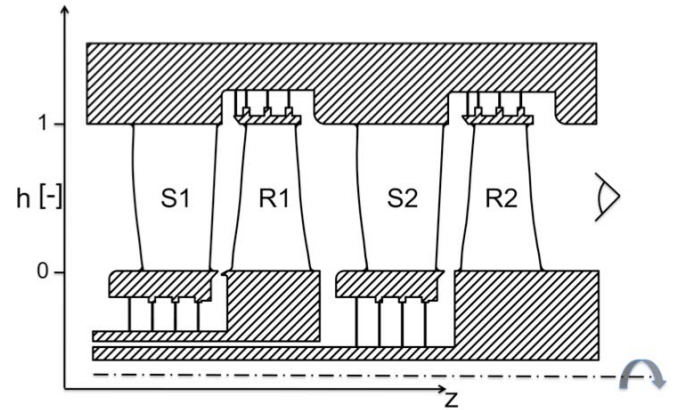


Figure 3: Schematic diagram of the two-stage axial turbine.

Parameter	HS stator	LS stator
Blade count Z_s	48	36
Axial chord* C_z [mm]	50	50
Chord length* C [mm]	66.3	77.4
Pitch* T [mm]	46.5	62.0
Blade span H [mm]	90	90
Aspect ratio $AR = H/C$ [-]	1.36	1.16
Solidity $\sigma = C/T$ [-]	1.43	1.25

Table 1: Geometric details of stator blades.

(* Indicates that the dimension is measured at 50% span)

Instrumentation

Both steady and unsteady flow field measurements were made. In the main flow, the steady flow field was measured with a 5-hole pneumatic probe (5HP) with a 0.9 mm head diameter, whereas the unsteady flow field was captured with the use of a 2-sensor Fast Response Aerodynamic Probe (FRAP), which has a 1.8 mm head diameter as shown in Figure 4. For measurements inside the cavity, a miniature 4-hole pneumatic probe (4HP) was used for the steady flow field together with a pair of miniature FRAP probes of 0.84mm head diameter for the unsteady flow field. Each miniature FRAP probe is one-holed; one miniature FRAP is yaw sensitive and the other is used for the pitch measurement. A detailed description of the two miniature probes can be found in Pfau et al. [22] The FRAP has a measurement bandwidth of 48 kHz. The measured flow parameters and their absolute uncertainties are listed in Table 3. Absolute uncertainties of the measured flow

quantities in Table 3 are expressed as a percentage of the calibration range for the angles, a percentage of the dynamic head for pressures and a percentage of the absolute Mach number for the velocity. The use of FRAP and pneumatic probes in the turbine facility ‘LISA’ has been detailed in several publications, including Lenherr et al. [23].

Rotor speed [RPM]	2750
Overall pressure ratio [-]	1.32
Mass flow [kg/sec]	7.87
Turbine inlet temperature [K]	310
Blade number count stage-1 (stator/rotor)	48/48
Blade number count stage-2 (stator/rotor)	36/48
Tip/hub diameter [mm]	800/620
Flow coefficient (stage-2) [-]	0.3
Loading coefficient (stage-2) [-]	1.0
Mach number (stator/rotor)	0.32/0.1
Reynolds number (rotor)	2×10^5

Table 2. Main parameters of the test case configuration based on the characteristics of the LS stator.

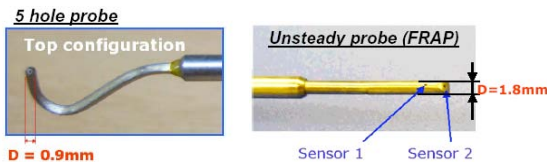


Figure 4: 5HP and 2-sensor FRAP measurement probes.

Probe measurements were made at the rotor exit and downstream of the LS stator. Measurements at the stator exit were made 6mm downstream of the stator at $h=1$. The measurement plane is located at $0.224C_z$ downstream of the 2nd stator’s trailing edge at midspan. The measurement grids consist of 48 points and 61 points evenly distributed in both radial and circumferential directions, respectively. The circumferential traverse was conducted over three LS stator pitches. Data are sampled at 200 kHz, which corresponds to 92 samples per blade passing period. A phase-lock data-averaging procedure was subsequently performed over 90 rotor revolutions.

	α	γ	P_t	P_s	M
FRAP	0.5°	0.7°	1%	1.2%	1%
5HP	0.3°	0.3°	1.8%	2%	0.06%

Table 3: Absolute uncertainties in probe measurements for a calibration range of yaw $\pm 30^\circ$ pitch $\pm 20^\circ$ and for a Mach number of 0.3. (uncertainties in pressure are expressed as a percentage of dynamic head, uncertainties in Mach number are expressed as a percentage of the absolute Mach number).

Numerical method

The numerical study presented in this paper was performed using the ANSYS CFX flow solver. The second stage of the turbine (Figure 5a) was meshed using an unstructured mesh with 8 million nodes, as shown in Figure 5b. The stator-rotor blade count ratio of the second stage is 3:4. As the periodicity is related to the stator-rotor blade count ratio, 30 degrees were meshed; i.e. three stator passages and four rotor passages. The y^+ values on the walls were all below 30. The flow solver was run in unsteady mode using the transient rotor-stator interface. The results of the steady simulations were used as initial conditions. As a convergence criterion a reduction of the maximum mean square value for the residual from 10^{-2} to 10^{-6} was used. The standard k- ϵ turbulence model with a turbulence intensity of 5% at the inflow boundary layer was employed. The experimentally measured mass-averaged total pressure, together with the flow angle distribution and the static temperature constituted the boundary conditions at the inflow, whereas at the outflow the measured static pressure distribution was used for the steady simulation, which provided a good initial solution. The circumferential boundaries are periodic and a no-slip condition was applied at the adiabatic walls.

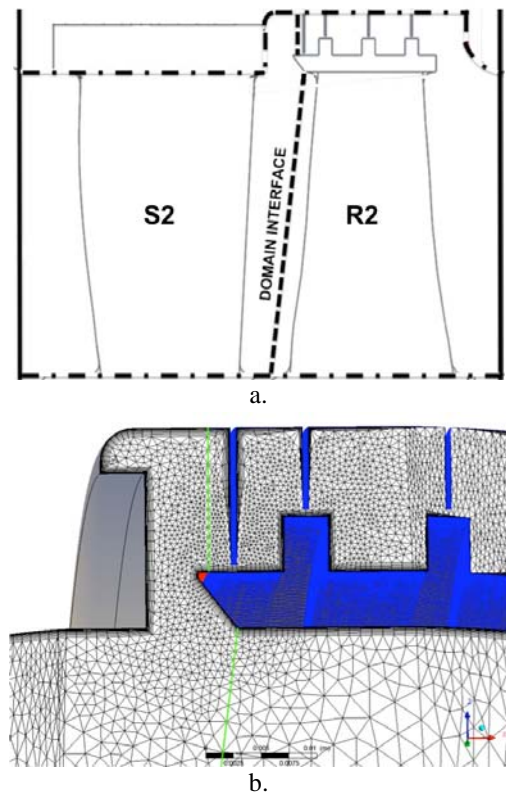


Figure 5: The simulation domain is bordered by the measurement planes, solid lines at stage inlet and outlet. The center line sketches the simplified fluid path without the stator hub cavity. The domain interface is indicated by the dashed line.

Validation

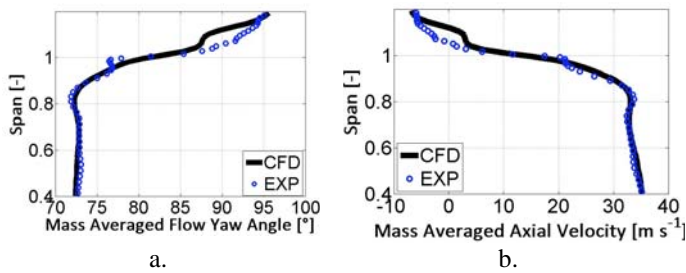


Figure 6: Comparison of experiment and CFD for (a) the pitchwise mass-averaged flow yaw angle distribution and (b) the pitchwise mass-averaged axial velocity distribution at stator exit.

Figure 6 shows the comparison of experimental and numerical data of the pitchwise mass-averaged flow yaw angle and axial velocity distribution at the stator exit. There is a very good agreement within 0.5 degrees for the yaw angle up to 0.95 of the span. The CFD does not predict the overturning of the flow close to the upper casing. Moreover, inside the cavity, because of the strong secondary flows, the difference between experimental and computed results rises by up to 5 degrees. The pitchwise mass-averaged axial velocity shows very good agreement over the blade span. The difference is within 1 m/s. Inside the cavity, although the trend is captured, the CFD predicts higher velocities.

RESULTS AND DISCUSSION

The experimentally measured stage efficiency for the three cases examined in this work is shown in Figure 7. Overall, the efficiency increases by 0.33% for the 14% CVR compared to the baseline case. A further reduction of 28% to the initial CV decreases the efficiency by 0.2% compared to the baseline case.

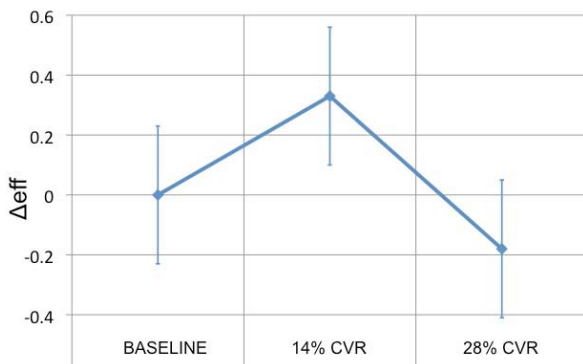


Figure 7: Δe_{eff} for the baseline, 14% CVR and 28% CVR. Efficiency of the baseline case with the initial cavity volume used as a reference.

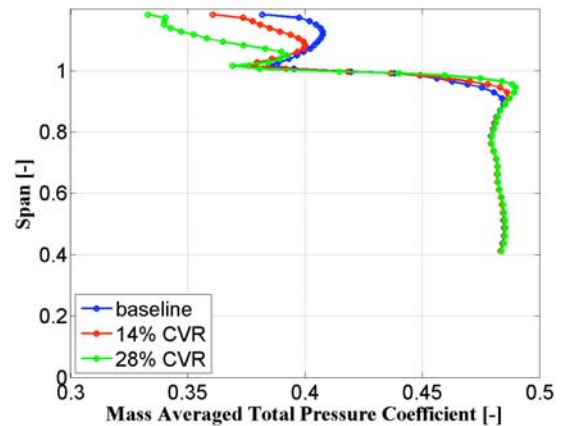


Figure 8: Experimentally measured pitchwise mass-averaged total pressure coefficient at stator exit.

The experimentally measured total pressure loss coefficient at stator exit for the three cases is presented in Figure 8. The total pressure coefficient is pitchwise mass-averaged. Above 100% span the measurements are of flow inside the cavity. The extension of the upper casing results in lower loss generation in the region where the boundary layer develops, from 0.9 – 1.0 span. The boundary layer that forms on the upper stator casing exits the stator blade passage and continues turning as long as the casing still exists, until it reaches the cavity entrance, where it experiences a sudden, shear-generating turn in the circumferential direction. An elongated platform provides the necessary boundary for the flow to continue overturning and therefore less shear is observed downstream of the stator exit, as shown in Figure 8. Inside the cavity, a reduced volume lowers the pressure, which in turn lowers the pressure difference and hence the driving force of the flow across the labyrinth between the inlet and exit cavities. Nevertheless, the leakage fraction derived as the ratio of leakage to main mass flow for the three cases examined, given in Table 4, does not vary significantly. The shortening of the cavity's axial length along with the CVR does not affect the amount of the leakage flow that finally escapes through the labyrinth as both CVR cases experience a leakage flow that differs by no more than 1.5% compared to that of the baseline. Moreover, the geometry changes of the cavity inlet do not affect the flow field below 90% of the blade span at stator exit.

Case	Baseline	14% CVR	28% CVR
Leakage fraction [%]	1.22	1.24	1.21

Table 4. Leakage fraction at inlet cavity.

Contrary to the trend observed at the stator exit, no trend is observed at the rotor exit. In Figure 9, the pitchwise mass-averaged flow pitch angle distribution at the rotor exit is presented. While there is a similarity between the baseline case and the 28% CVR case, the flow field is significantly

different for the 14% CVR case. The tip passage vortex of the 14% CVR case is considerably reduced in both size and magnitude and seems not to affect the flow field at lower spans unlike the two other cases, as shown in Figure 9. Large non-uniformities are present for the baseline case and the 28% CVR across the whole span, notably at 0.7 and 0.4-0.6. A larger vortex at the rotor exit circulates more mass flow and ultimately leads to more mass flow being exchanged. A larger vortex, manifested by the larger mass-averaged pitch angle in Figure 9, occupies more space in the tip section of the blade as it extends to lower span locations. Therefore, the flow underneath is squeezed. Additionally, due to more mass flow being handled by the tip passage vortex, the formation of smaller vortices in series across the span is facilitated, giving larger mass-averaged pitch angle oscillation at mid-span. While the shortening of the axial inlet cavity gap is beneficial in terms of loss generation at rotor inlet, the flow field at rotor exit seems to cancel out that benefit. In the following, the results of the unsteady computational analysis are presented in order to examine this flow behavior in more detail.

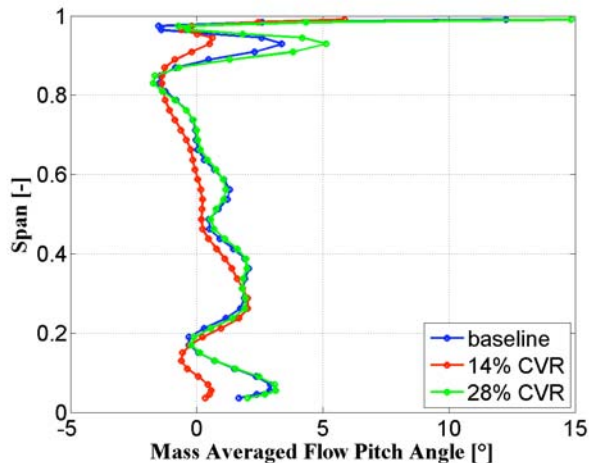


Figure 9: Experimentally measured pitchwise mass-averaged flow pitch angle at rotor exit.

Overall, three different phenomena affect the flow field in the cavity area. Firstly, there is a captive vortex in a driven cavity. As the flow exits the stator passage at an angle to the blade and passes underneath the cavity, it drives the flow of the cavity into a circular motion. Secondly, the flow that has been turned within the stator passage tends to move upwards on the pressure side of the stator blade and downwards on the suction side. Once the opposite moving flows reach the cavity entrance they interact with the cavity flow. Lastly, the pressure side leg of the horseshoe vortex that has already started to form on the rotor blade is highly affected by the interaction of the upward moving jet with the cavity flow. Although the aforementioned are valid for the baseline case and the 14% CVR case, they are not observed in the 28% CVR case, since there is no vortex formation within the cavity due to the lack of the necessary axial gap. The cavity volume impacts drastically on the flow

kinematics of the cavity itself. In Figure 10, the inflow and outflow for the three inlet cavity configurations are presented. In the upper row in Figures 10a, 10b and 10c, a meridional cut of the inlet cavity is shown at the instant in time when they are on the pressure side of the rotor blade, whereas on the row below, Figures 10d, 10e and 10f show the inlet cavity flow after the rotor leading edge has passed. The 2D plots are colored with radial velocity and secondary flow velocity vectors are projected onto them. Positive radial velocity points upwards and inside the cavity. The baseline case, shown in Figures 10a and 10d, experiences a vortex that dominates the entire cavity. The core is located in the middle of the upper half of the cavity at $h=1.11$ and stays steady during in and outflow. The vortex is fed by high-pressure fluid originating from the pressure side of the stator blade. With a $0.17c$ extension of the stator casing and during inflow the vortex migrates slightly higher to $h=1.12$, but it remains unaffected in terms of size, as seen in Figure 10b. Nevertheless, during outflow (Figure 10e), an additional vortex appears at the lower part of the cavity at the interaction zone. Right after the rotor blade trailing edge passes by, the newly formed vortex interacts with the main flow at a ratio of 3:4 with the rotor pitch. It disappears when close to the pressure side of the rotor blade, as high-pressure fluid, coming from the stator and influenced by the potential flow field of the rotor is redirected upwards and inside the cavity. The situation undergoes a dramatic change when the cavity inlet is reduced even further to $0.34c$, as in Figures 10c and 10f. The flow is characterized by a total absence of a toroidal vortex inside the cavity. When at the pressure side of the rotor blade, the cavity is washed out along its whole radial length by a strong upward-moving jet. What used to form the toroidal vortex now appears to be attached to the upper axial wall of the cavity with considerably reduced size and strength. On the suction side of the blade a downward moving jet dominates the cavity. Two small corner vortices appear attached to the shroud. An initially large vortex that was axially confined finally splits into two smaller vortices of the same rotational sign.

For both the cases where the toroidal vortex is formed within the cavity, the fluid will exit the cavity when the low-pressure fluid originating from the suction side of the stator blade passes underneath. By extending the upper casing platform by 17% of the axial cavity gap, the flow is hindered from exiting the cavity and this happens at a location further downstream. The remaining 83% of the axial cavity length has to accommodate both the ingress as well as the egress of the flow. The large vortex in the baseline case extends inside the main flow contrary to the 14% CVR case, where the lower branch of the bifurcated vortex, being smaller in size, does not penetrate into the main flow, as shown in Figure 11. Bearing in mind that in both the baseline and 14% CVR cases the mass flow handled is within the limited range of 1.5% based on the baseline leakage flow, the vortex of the lower half of the cavity of the 14% CVR case will only circulate half of the mass flow compared to the baseline case.

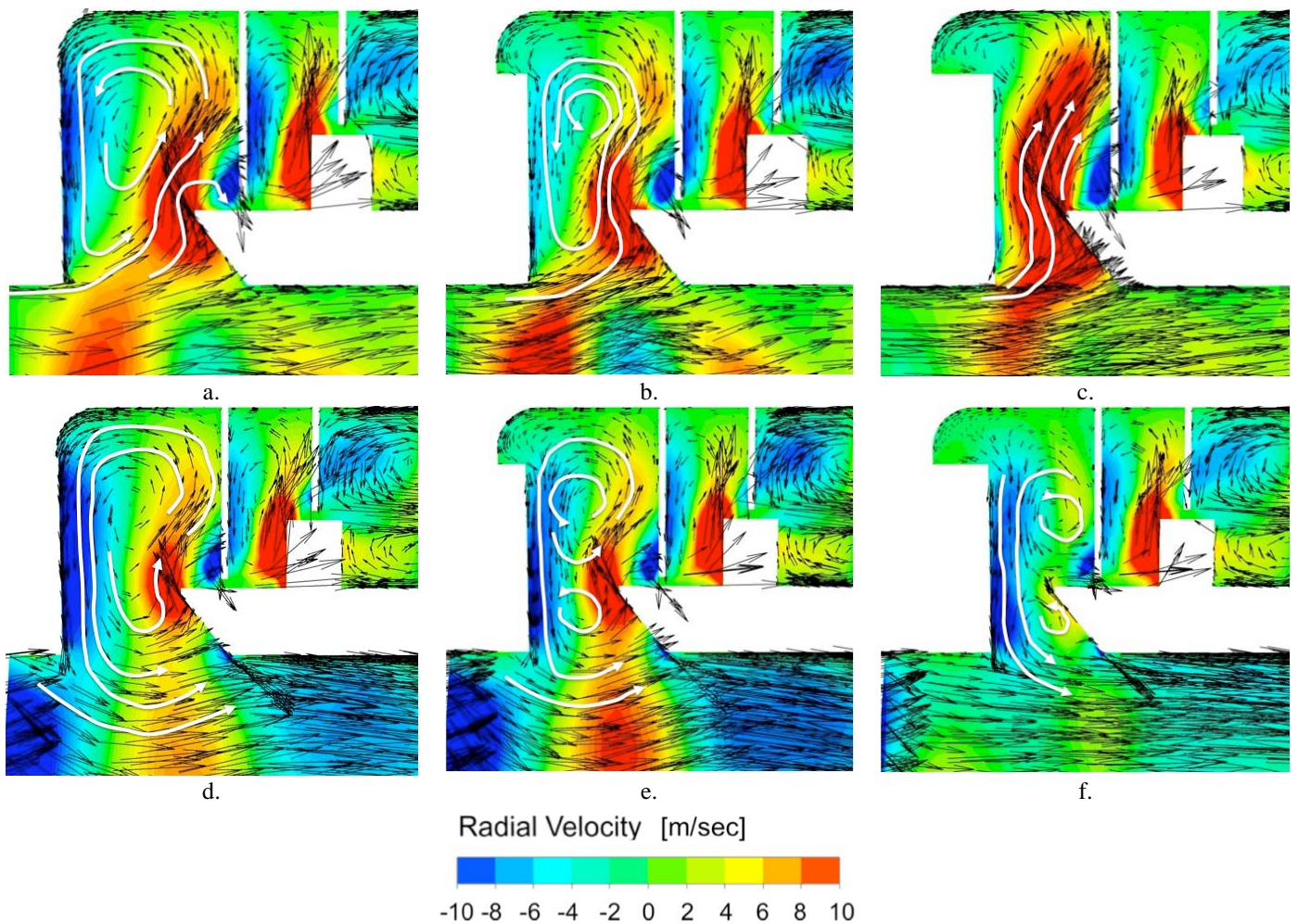


Figure 10: CFD simulations of the inflow for the cases (a) baseline, (b) 14% CVR, and (c) 28% CVR; and the outflow for the cases (d) baseline, (e) 14% CVR, and (f) 28% CVR. The simulations show a meridional cut on the pressure for (a), (b) and (c), and on the suction side for (d), (e) and (f) of the rotor blade. The planes are colored with radial velocity and the secondary flow vectors are projected onto them. The flow path is denoted by white lines.

The other half is trapped in the upper branch. Therefore, half the mass flow will be involved in the mixing process at the interaction zone during outflow. When the axial cavity length is reduced even further, the gap size is insufficient for a vortex to be formed to handle the leakage mass flow. A jet appears instead and flushes the cavity in and out.

Cavity flows at the interaction zone are influenced both by the stator and the rotor. The stator and the rotor have the same influence zone extending to 60% of the initial axial cavity gap on either side. In Figure 12, the mass fluxes at a point in time are plotted over the repeating stage and the axial cavity entrance length at the cavity inlet. Red colored areas show the radially upward-moving fluid, whereas the blue colored areas represent the fluid egress. On the stator side of the plot 3 peaks and troughs can be identified, which are related to the 3 stator blades of the repeating sector, whereas on the other side 4 rotor blades interact with the cavity entrance. The superimposition of the upward-moving

fluid originating from the pressure side of the stator blade on the fluid that is redirected radially upwards due to the rotor potential flow field occurs in the middle of the cavity for the baseline case, and is shown with a solid circle in Figure 12a. Shortening the axial cavity length by $0.17c$ reduces the stator influence on the interaction zone. The flow is more rotor-driven and the maximum mass flux ingress occurs further downstream due to the shortened length, shown by the solid circle in Figure 12b. In the 28% CVR case, Figure 12c, the influence of the stator has completely disappeared and the flow is only rotor-driven along its whole length. This is evident as the four peaks and troughs are clearly identifiable as originating from the rotor potential flow field. The reduced streamwise direction of the flow impacts negatively on the efficiency as negative incidence is imposed on the rotor blade. The ratio of the cavity's axial-to-radial wall length determines the flow kinematics in terms of vortex size. A ratio of 0.44 in the baseline case

allows the formation of one large vortex that dominates the entire cavity. While maintaining the main flow velocity at the stator exit, a decrease of the ratio to 0.33 in the 14% CVR case forces the vortex to be broken up into two smaller, vertically aligned vortices that would maintain their characteristics if there was no intervention by an external force. Although the overall mass flux along the cavity's axial gap follows an identical radial flow pattern, there is an area in the 14% CVR case, highlighted by the solid black line in Figure 12b, where the radial mass flux is increased by 23% because of the smaller axial gap compared to the baseline case. As a result of this increased mass flux, the bifurcated vortex reconnects.

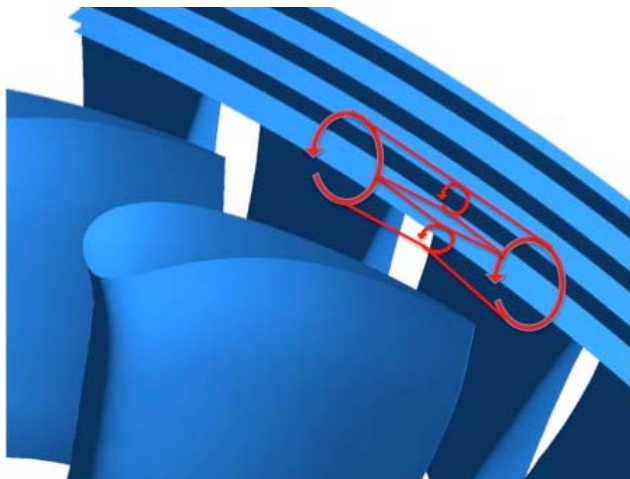
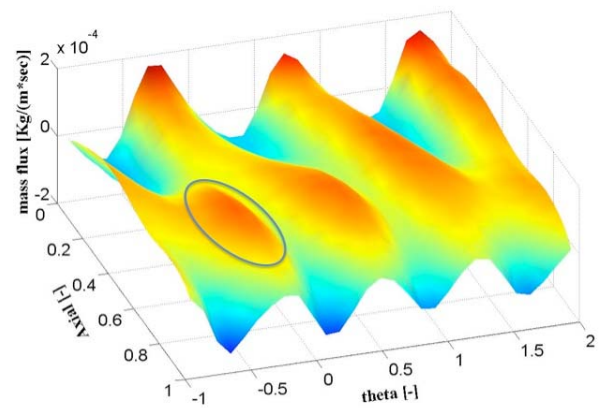


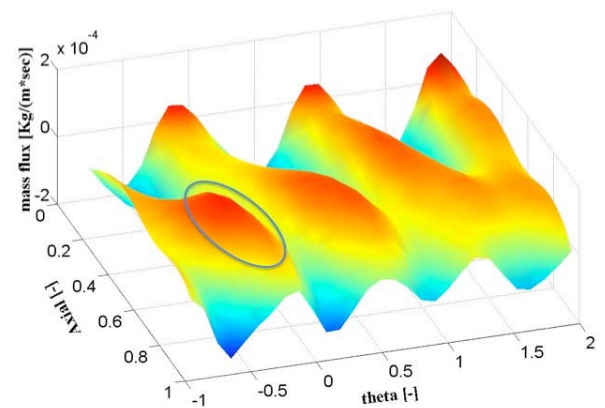
Figure 11: Schematic of vortex bifurcation during outflow and reconnection during inflow for the 14% CVR case

The maximum mass flow ingress occurs at a more downstream position, at $0.72c$ for the 14% CVR, as compared to the baseline case where the largest inflow is in the middle of the axial gap. However this inflow is spread over the larger axial cavity length, as can be seen in Figure 13. The maximum inflow for the 28% CVR case lies between the two previous cases, at $0.62c$ with its maximum being a 54% increase relative to the baseline case. With an axial-to-radial wall length ratio of 0.22 for the 28% CVR case, the magnitude of the peaks of the mass flow cavity ingress show that the magnitude of the maximum mass flow increases monotonically with the ratio of the axial-to-radial cavity wall lengths.

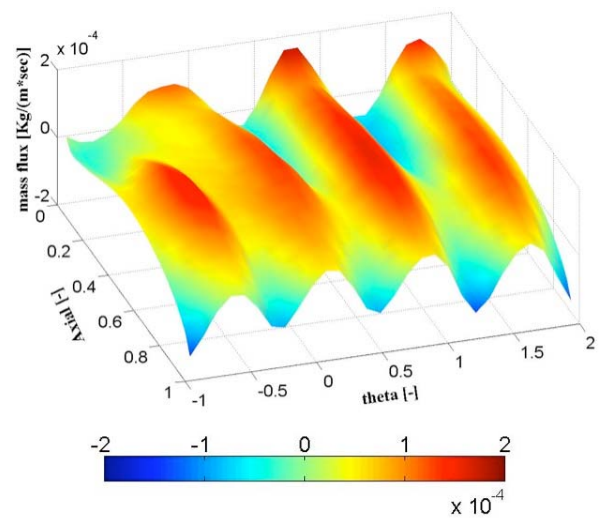
The greater mass flow exchange at the interaction zone for the baseline case results in a larger tip passage vortex being formed on the pressure side of the rotor blade. The downward-moving flow of the stator suction side is enhanced by the egress of the cavity fluid. This flow, together with the upward moving fluid, continues along a streamwise path until it intersects with the rotor leading edge. This pair of fluids that move opposite to each other can potentially evolve to form a vortex with the same sign of rotation as the pressure side leg of the horseshoe vortex.



a.



b.



c.

Figure 12: CFD predicted instantaneous mass fluxes at cavity inlet for (a) baseline, (b) 14% CVR case, and (c) 28% CVR case. Red colored areas show fluid moving upwards, blue colored areas show fluid exiting the cavity

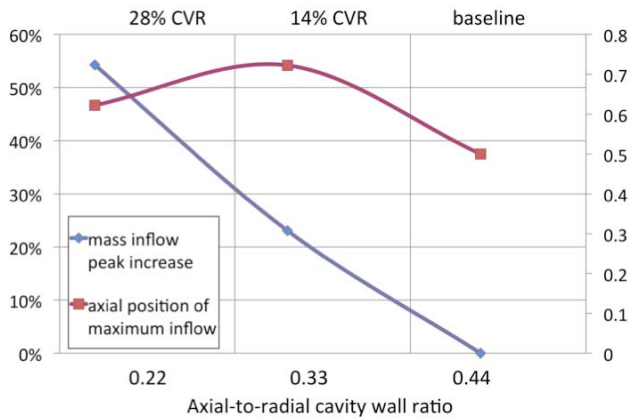


Figure 13: CFD predicted mass inflow peak increase relative to the baseline case, blue line, axis on the left, and non-dimensionalized axial position where the maximum inflow occurs, red line, axis on the right.

The interaction of these two vortices leads to the strengthening of the horseshoe vortex. On the other hand, a shortening of the available axial gap by $0.17c$ leads to a smaller mass flow egress. The vortex that resides in the lower half of the cavity handles only half the mass flow compared to the toroidal vortex of the baseline case. Therefore, less mass flow is being re-injected back into the main flow and with a swallow angle as the smaller vortex of the 14% CVR case does not penetrate into the main flow. As a result, a weaker tip passage vortex will be formed. A further reduction of the available cavity's axial length completely eliminates the presence of the toroidal vortex, as already mentioned. Since the amount of mass flow that finally escapes through the labyrinth over the 2nd stage rotor remains the same, the absence of a vortex that would smoothly regulate the mass flow exchange at the interaction zone is now replaced by a strong jet that fills the cavity and subsequently exits from the cavity. The flow that exits the stator passage is redirected upwards once it is in front of the pressure side of the rotor blade. All the mass flow that was to enter the cavity mainly through the middle of the cavity's axial gap now enters the cavity, and fills the entire axial cavity gap, as seen in Figure 14. The inflow region is now located circumferentially closer to the rotor blade, contrary to the circumferentially elongated and axially-centered inflow pattern. Thus it covers one-third of the stator pitch, as opposed to half for the baseline and 14% CVR cases (Figure 14a, 14b). The outflow region has also been circumferentially moved towards the suction side of the stator blade. The inflow region occupies circumferentially less area and a stronger jet is thus formed. Fluid originating from the lower stator blade span positions is also trapped in this upward movement and is transported downstream to the rotor leading edge. The pressure side leg of the horseshoe vortex is re-enforced, as more mass flow becomes involved, because of this upward movement of the fluid.

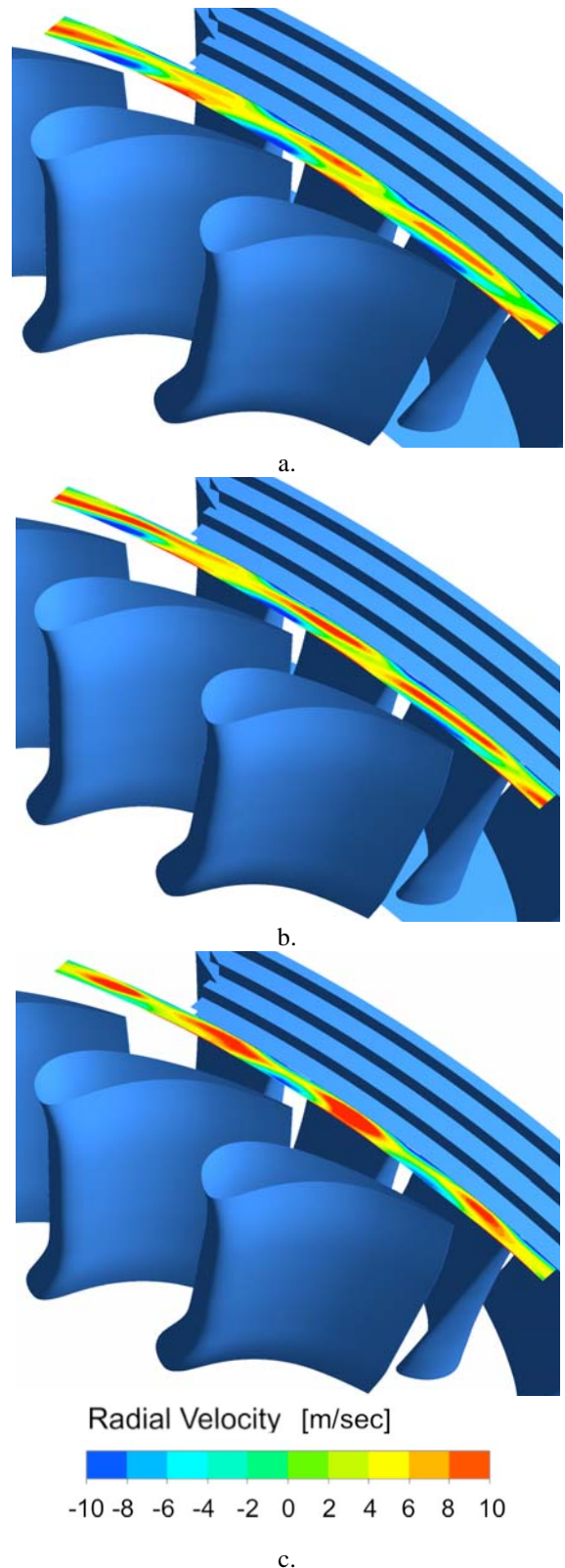


Figure 14: CFD predicted inflow and outflow at cavity entrance for (a) baseline case, (b) 14% CVR case and (c) 28% CVR case. The cavity inlet is colored to show the radial velocity. Red indicates fluid moving upwards into the cavity; blue indicates fluid that exits the cavity

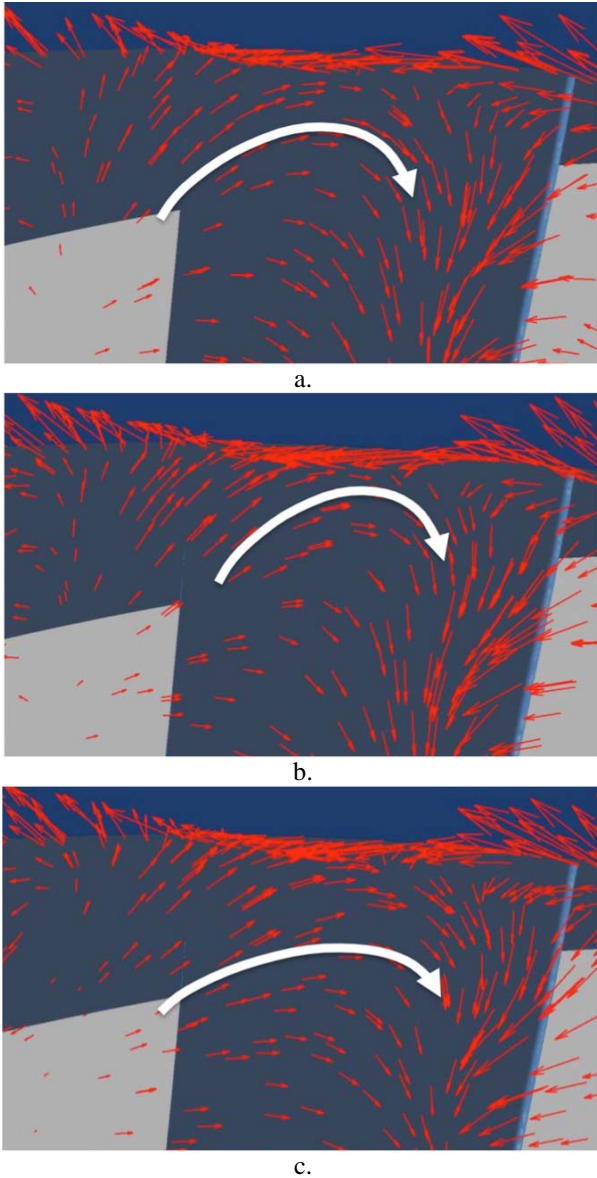


Figure 15: CFD predicted tip passage vortex at rotor exit as seen from a downstream location for (a) baseline case, (b) 14% CVR case and (c) 28% CVR case.

In Figure 15, the tip passage vortex is visualized using secondary flow vectors on the exit plane downstream of the rotor exit. Although there is a relative resemblance between the baseline and 28% CVR cases in terms of the position of the vortex core and its magnitude, the 14% CVR case is substantially different. The vortex core in the 14% CVR case is displaced upwards closer to both the casing and the suction side of the blade. A more energetic vortex at the rotor exit will tend to deviate more from the blade exit angle and expand in size, therefore enabling more mass flow into its circular motion (Figure 15a, 15c). The smaller magnitude of the tip passage vortex in the 14% CVR case is also visualized in Figure 16 by the use of streamlines. Streamlines originating from 3 different span locations at rotor inlet (yellow at 99%, red at 95% and green at 90% of the blade span) clearly show the smaller vortex formed at the rotor exit for the 14% CVR case compared to the

baseline and 28% CVR cases, Figure 16b. Moreover, the strong upward movement of fluid originally at lower span locations is especially evident for the 28% CVR case shown in Figure 16c. As more mass flow is involved in the rotor tip passage vortex for the 28% CVR case, a stronger and more energetic vortex forms, that migrates towards the pressure side of the neighboring rotor blade as it convects through the rotor passage.

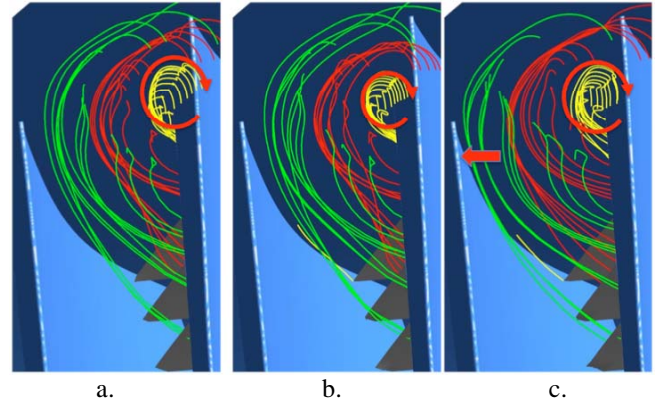


Figure 16: CFD predicted tip passage vortex visualized with the use of streamlines at rotor exit for (a) baseline case, (b) 14% CVR case and (c) 28% CVR case. The streamlines originate from three planes at rotor inlet: yellow 99%, red 95% and green 90% of the blade span. Upstream view.

While the extension of the upper stator casing platform positively affects the flow field at stator exit, the simultaneous cavity volume reduction acts beneficially only as long as the vortex still forms inside the cavity. Moreover, the flow field at the interaction zone greatly influences the formation of the rotor tip passage vortex, which is fed by fluid originating from the interaction zone. A large cavity vortex that extends beyond the limits of the cavity into the main flow for the baseline case, as well as the formation of jets because of the insufficient axial gap to form a vortex in the 28% CVR case, lead to larger tip passage vortices and thus also lead to a work extraction deficit over the rotor. Overall, the rotor inlet cavity volume and its axial inlet length have a profound impact on efficiency through their influence on the path of the cavity flows and therefore the mixing procedure at the interaction zone. The cavity volume and length scale should allow for a beneficial cavity vortex to be formed that continually regulates the in and outflows. A rectangular cavity shape that initiates the break-up of an initial larger vortex into two smaller vortices leads to efficiency gains through decreased mass flux oscillations at the interaction zone and smoother re-injection angles. An axial to radial cavity wall length ratio of 0.33 was proved here to support the presence of two smaller vortices. Nevertheless, since the vortex size is related to its frequency, a designer should carefully couple the cavity size with the stator exit velocity, which is the vortex driving mechanism.

CONCLUSIONS

This paper examines the mixing process occurring at the interaction zone between the cavity and main flows. A series of experiments has been carried out to investigate the influence of three different rotor inlet cavity volumes along with an extension of the upper casing stator platform on stage efficiency. Experimental results were supported by computational analysis.

The initial cavity volume of the baseline case was reduced by 14% and 28%. This was achieved by a uniform extension of the upper stator casing platform by 17% and 34% of the initial axial cavity length. The extension of the stator casing allows for a greater overturning of the flow before the cavity entrance is reached and the flow turns in a circumferential direction. The smaller the jump experienced by the flow, the smaller the losses in the tip section at the exit of the stator blade. Inside the cavity, the decrease of the axial cavity's length impacts on the flow kinematics and the formation of the vortex itself.

A 14% cavity volume reduction results in the break-up of the single vortex during inflow into two smaller vortices during outflow, as compared to the presence of the single vortex at all times for the baseline case. The smaller vortex in the lower half of the 14% CVR case causes less mixing at the interaction zone as it circulates less fluid. Furthermore, it improves the re-entry of the flow that takes place at a smoother angle, as the vortex does not penetrate into the main flow. Thus, it does not support the pressure side leg of the rotor horseshoe vortex at its onset as much as in the baseline case. A further reduction of the cavity volume completely changes the behavior of the cavity flows, which are characterized by the absence of any toroidal vortex and which are now replaced by strong in and outflow jets. Greater mixing due to the strong jets as well as a larger rotor tip passage vortex, facilitated by the strong in and out flow, are present. While the impact on stage efficiency is positive and an increase of 0.33% is observed compared to the baseline case for the 14% CVR, the further reduction leads to an efficiency deficit of almost 0.2% relative to the baseline case.

This study suggests that the reduction of the rotor inlet cavity volume through the extension of the stator casing platform acts beneficially on stage efficiency till the point when the toroidal vortex of the cavity breaks down due to a lack of the necessary axial distance that allows the latter to form.

ACKNOWLEDGMENTS

The authors acknowledge the significant contributions of Mr. Tsuguhisa Tashima, Dr. Tadashi Tanuma, Mr. Takashi Sasaki and Dr. Hideo Nomoto of Toshiba in the design and development of the inlet cavity configurations. We also thank the Toshiba Corporation for permission to publish this data.

REFERENCES

- [1] Egli, A., 1935, "The Leakage of Steam Through Labyrinth Seals," Transactions of the ASME, Vol. 57, pp. 115-122
- [2] Traupel, W., 1973. Thermische Turbomaschinen. Springer-Verlag, Berlin
- [3] Wallis, A. M., Denton, J. D., Demargne A. A. J., 2001, "The Control of Shroud Leakage Flows to Reduce Aerodynamic Losses in a Low Aspect Ratio Shrouded Axial Flow Turbine," ASME J. of Turbomachinery, Vol. 123, pp. 334-341
- [4] Rosic, B. and Denton, J. D., 2008, "Control of Shroud Leakage Loss by Reducing Circumferential Mixing," ASME J. of Turbomachinery, Vol. 130, pp. 021010-1 – 021010-7
- [5] Mahle, I., 2010, "Improving the Interaction Between Leakage Flows and Main Flow in a Low Pressure Turbine," ASME GT2010-22448
- [6] Denton, J. D., 1993, "Loss Mechanisms in Turbomachines," The 1993 IGTI Scholar Lecture, ASME J. of Turbomachinery, Vol. 115, pp. 621-656.
- [7] Peters, P., Giboni, A., Menter, J. R., Pfost, H., Wolter, K., 2005, "Unsteady Interaction of Labyrinth Seal Leakage Flow and Downstream Stator Flow in a Shrouded 1.5 Stage Axial Turbine," ASME GT2005-68065
- [8] Anker, J. E., Mayer, J. F., Casey, M. V., 2005, "The Impact of Rotor Labyrinth Seal Leakage Flow on the Loss Generation in an Axial Turbine," Proc. IMechE, Part A: J. Power and Energy Vol. 219, pp. 481-490
- [9] Gier, J., Stubert, B., Brouillet, B., de Vito, L., 2005, "Interaction of Shrouded Leakage Flow and Main Flow in a Three-Stage LP Turbine," ASME J. of Turbomachinery, Vol. 125, 649-658
- [10] Pau, M., Cambuli, F., Mandas, N., 2008, "Shroud Leakage Modeling of the Flow in a Two-Stage Axial Test Turbine," ASME GT2008-51093
- [11] Adami, P., Martelli, F., Cecchi, C., 2007, "Analysis of the Shroud Leakage Flow and Mainflow Interactions in High-Pressure Turbines Using an Unsteady Computational Fluid Dynamics Approach," Proc. IMechE, Part A: J. Power and Energy Vol. 221, pp. 837-848
- [12] Hunter, S. D., Manwaring, S. R., 2000, "Endwall Cavity Flow Effects on Gas Path Aerodynamics in an Axial Flow Turbine: Part 1 - Experimental and Numerical Investigation," ASME 2000-GT-651
- [13] Vakili, A. D., Meganathan, A. J., Michaud, M., Radhakrishnan, S., 2005, "An Experimental and Numerical Study of Labyrinth Seal Flow," ASME GT2005-68224
- [14] Rhode, D. L., Johnson, J. W., Broussard, D. H., 1997, "Flow Visualization and Leakage Measurements of Stepped Seals: Part 1 – Annular Groove," ASME J. of Turbomachinery, Vol. 119, pp 839-848
- [15] Rhode, D. L., Johnson, J. W., Broussard, D. H., 1997, "Flow Visualization and Leakage Measurements of Stepped Seals: Part 2 – Sloping Surfaces," ASME J. of Turbomachinery, Vol. 119, pp. 844-848
- [16] Curtis, M. E., Denton, D. J., Longley, P. J., Budimir, R., 2009, "Controlling Tip Leakage Flow Over a

Shrouded Turbine Rotor Using an Air-Curtain,” ASME GT2009-59411

[17] Schlienger, J., Kalfas, A. I., Abhari, R. S., 2004, “Vortex-Wake-Blade Interaction in a Shrouded Axial Turbine,” ASME GT-2004-53915

[18] Pfau, A., Schlienger, J., Kalfas, A. I., Abhari, R. S., 2003, “Unsteady Flow Interactions within the Inlet Cavity of a Turbine Rotor Tip Labyrinth Seal,” ASME GT2003-38271

[19] Pfau, A., Kalfas, A. I., Abhari, R. S., 2004, “Making use of Labyrinth Interaction Flow,” ASME GT2004-53797

[20] Schlienger, J., Pfau, A., Kalfas, A. I., Abhari, R. S., 2003, “Effects of Labyrinth Seal Variation on Multistage Axial Turbine Flow,” ASME GT2003-38270

[21] Tashima, T., Sasaki, T., Kalfas, A. I., Abhari, R. S., 2007, “Blade Loading Influence on Unsteady Flow Interactions in Axial Steam Turbines,” ASME GT2007-27452

[22] Pfau, A., Schlienger, J., Kalfas, A. I., Abhari, R. S., 2003, “Unsteady, 3-Dimensional Flow Measurement using a Miniature Virtual 4-sensor Fast Response Aerodynamic Probe (FRAP),” ASME GT2003-38128

[23] Lenherr, C., Kalfas, A. I., Abhari, R. S., 2007, “A Flow Adaptive Aerodynamic Probe Concept For Turbomachinery,” Meas. Sci. Technol. Vol. 18, pp. 2599-2608